

Hopping mechanisms, photoluminescence studies toward highly efficient UV-responsive $\text{Pr}_2\text{MgTiO}_6$ photocatalyst

Moumin Rudra*, T. K. Bhowmik, H. S. Tripathi, R. A. Kumar, R. Sutradhar, and T. P. Sinha
Department of Physics, Bose Institute, 93/1, A. P. C. Road, Kolkata, India 700009.

*Corresponding author:

Address: *Department of Physics, Bose Institute, 93/1, A. P. C. Road, Kolkata, India 700009.*

Email: iammoumin@gmail.com

Phone: +91-33-23031194, +91-9477398318 (Mobile).

ABSTRACT

Titanium based-perovskites have got surprising attraction due to their environment-friendly photocatalysts behavior. The Rietveld refinement of X-ray diffraction (XRD) pattern authenticates the orthorhombic *Pnma* structure of $\text{Pr}_2\text{MgTiO}_6$ (PMT). The $\text{Pr}^{3+}\text{-Ti}^{4+}$ intervalence charge transfer process plays an important role inside PMT. The dc conductivity shows a change in the hopping mechanism from nearest-neighbor hopping to a variable range hopping due to the activation energy reduction. This change in the hopping mechanism is well supported by both the relaxation time and impedance data in PMT. The constant phase element (CPE) model is utilized to fit impedance plots. The photocatalytic activity of PMT was performed under UV irradiation with the help of degradation kinetics of organic pollutants. Also, the photocatalytic efficiency of recycled and reused PMT finds 91.2% after 5th cyclic runs. The calculated band-gap is found to be 3.58 eV.

KEYWORDS: Perovskite, Photoluminescence, Electrical Conductivity, Impedance Spectroscopy, Photocatalysts, Band-gap.

1. INTRODUCTION

Today, our main concern about global pollution, as day by day global industrialization developed rapidly. Organic pollutants are unable to remove completely using our traditional water treatment technology [1,2]. Only photocatalysts can overcome this problem, as it uses solar energy directly and it is also environment friendly. The titanium (Ti) based oxides are the ideal photocatalysts and widely used as photodegradation of organic pollutants [3-7], hydrogen production by water splitting [8], gas sensors [9], and solar cell [10]. Now a day, with increasing global civilization, we are searching for a material which has not only photodegradation power but also has different interesting properties. In recent years, Shawky et. al. reported about the photocatalytic performance of Ag/LaTiO₃ can retain 96% after fifth cycle [11]. This reusability and effective photocatalytic performance suggests RETiO₃ [RE = rare-earth lanthanides] is an ideal host material [12 - 15].

Previous reports on the RETiO₃ lanthanide-based perovskites show low-temperature Jahn–Teller cooperative distortions, which are characteristics of localized electrons, which can affect both the valences of RE and Ti cations results in improvement of transport and optical behaviors of material [16]. Also in RETiO₃, the Ti⁴⁺ 3d⁰ orbital plays an important role to constitute the conduction band of the material [17]. Concerning other perovskites [18], an attractive structure makes La₂MgTiO₆ an ideal host material [19]. However, La is now being replaced by Pr as the electronic configuration of Pr matches with that of La and this replacement opens the Pr³⁺–Ti⁴⁺ intervalence charge transfer (IVCT) process in the material will influence the electron-hole population and further improve the transport properties of the material. Also, Pr³⁺ has a unique 4f² electronic configuration, which affects interesting properties in different applied areas like lighting devices [20], up-conversion areas [21], in-vivo targeted bio-imaging [22], etc. Also, another literature on Pr₂NiTiO₆ [23] suggests this type of material is also exhibits better electrical transport properties. In this work, the

correlations between the Pr³⁺ and Ti⁴⁺ based structural factors, optical, and transport properties are discussed.

The bulks and grain-boundaries (*Gbs*) are the two main constituents, which make the material microstructures. In this study, we have used impedance spectroscopy to investigate the electrical transport characteristics associated with the bulks and *Gbs* contributions in Pr₂MgTiO₆ (PMT). Various hopping models (mobility activated charge carriers) have been presented to report the hopping mechanisms for DPO systems. Nearest-neighbour hopping is a type of hopping mechanism in which single-valued activation energy is involved, which contributes the carriers to hop on the adjacent neighbor site. Another type of hopping mechanism is Mott's variable range hopping (MVRH) mechanism, which occurs at low temperatures due to lowering activation energy with the decrease in temperature [24]. No attempt has been made to study the electrical transport properties as well as the optical and photochemical properties of the perovskite oxide PMT.

2. EXPERIMENTAL

2.1. MATERIALS AND METHODS

PMT in powder form was synthesized by a standard solid-state synthesis technique at 1573 K in the air for 14 hrs. using Pr₂O₃ (Sigma-Aldrich, 99.9%), MgO (Merck, 99%), and TiO₂ (Merck, 99.99%) as the ingredient materials. The polyvinyl alcohol (PVA) (5%) was added with the calcined powders and the mixture was pressed inside the cylindrical pelletizer. The pressed pellets were sintered at 1623 K to obtain dense PMT pellets with thickness, $d \approx 1$ mm & diameter ≈ 8 mm. The crystallographic structure of PMT was studied using a powder X-ray diffractometer (Rigaku Miniflex II) [20 kV, 15 mA, Cu- K_{α} ($\lambda = 1.5406 \text{ \AA}$) radiation] in the 2θ range of $10^{\circ} - 80^{\circ}$ by the scanning rate of 0.02° per step at room temperature. A dual-

position graphite diffracted beam monochromator has been used with a scintillation counter detector. The collected XRD data were refined with the help of the FULLPROF program using the Rietveld method [26]. During the Rietveld refinement, the pseudo-Voigt functions were used to fit peak shapes and the background was fitted using a 6-coefficient polynomial function. The microstructural image of the sintered pellet was captured using a scanning electron microscope (SEM) (FEI Quanta 200). JASCO FP 8500 was used to measure photoluminescence spectra. Shimadzu UV 2401 was used to collect the UV-vis spectrum. The Fourier transform infrared (FTIR) spectrum of PNT was recorded in transmittance mode within the range from 390 cm^{-1} to 2000 cm^{-1} with Perkin Elmer Spectrum 1000. The impedance spectroscopy study of the sintered pellet was measured in the temperature range from 300 K to 700 K (frequency range $\approx 45\text{ Hz}$ to 5 MHz), using an LCR meter (HIOKI – 3532, Japan). Before starting the experiment, both bases of the measuring pellet were cleaned and the contacts were prepared from the thin silver paste. The real (ϵ') and imaginary (ϵ'') parts of the complex dielectric constant ϵ^* ($=\epsilon' + j\epsilon''$, where $\epsilon' = C_s/C_0$ and $\epsilon'' = \mathfrak{G}/\omega C_0$) were obtained from the capacitance (C_s) and the conductance (\mathfrak{G}), whereas the real (Z') and imaginary (Z'') parts of the complex impedance Z^* ($=Z' - jZ''$, where $Z' = Z\cos\phi$ and $Z'' = Z\sin\phi$) were obtained from the impedance (Z) and the phase angle (ϕ) [where ω is the angular frequency ($\omega = 2\pi\nu$), ν is the measured frequency and $j = \sqrt{-1}$). $C_0 = \epsilon_0 A/d$ is the parallel plate capacitance of empty cell, A is the base area and d is the thickness of pellet]. The ac electrical conductivity $\sigma (= \mathfrak{G}d/A)$ was measured from the \mathfrak{G} . The photocatalytic activity was measured through the degradation of organic pollutant Rhodamine B (Rh-B) using a UV lamp. Before the UV lamp is on, 0.1 mg of sample was added with 100 ml of Rh-B (5 mg/L) solution. The solution is mixed in a dark cool bath to attain absorption-desorption equilibrium for 2 hr. In every 10 min interval, a Milex syringe (filter of $0.22\text{ }\mu\text{m}$) was used to take 3 ml of solution from the solution bath for UV-Vis spectroscopy.

2.2. COMPUTATIONAL METHODS

The electronic structure of PMT has been calculated using the density functional theory (DFT) as implemented in the WIEN2k [25] package. The full potential linearized augmented plane wave (FP-LAPW) method is used to solve the Kohn-Sham equations. Firstly, the generalized gradient approximation (GGA) is taken as an exchange and correlation function to optimize the crystal structure. But it does not create any band-gap energy in the electronic structure because of the presence of the strongly correlated f-states of the Pr atom and d-states of the Ti atom. So, GGA along with the Coulomb repulsion, U (GGA+ U) is finally adopted to optimize the structure and further calculations. However, the supercell has been formed with a size of $2 \times 1 \times 1$ of lattice vectors, where one-unit cell consists of Mg atom and other Ti. The muffin-tin radii (RMT) for Pr, Mg, Ti, O are 2.48, 1.79, 1.88, and 1.70 a.u respectively. The energy cut off ($RMT \cdot k_{max}$) is set to -8 Ry to core states from the valance states. The k-space integration has been carried out with 500 k-points over the whole Brillouin zone. The Hubbard parameter ($U_{eff} = U - J$) is taken to 6 eV for Pr-4f states and 3 eV for Ti-3d states, where the J is set to zero. To achieve the self-consistency solutions, the energy and charge convergence criteria are set to 10^{-4} Ry and 10^{-3} e. After optimizing the crystal structure, the band structure and density of states (DoS) have been calculated for PMT double perovskite.

3. RESULTS AND DISCUSSION

3.1. X-RAY DIFFRACTION ANALYSIS:

The refined XRD pattern of the calcined powder of PMT at RT is shown in Fig.1 (a). The good quality of the refinement is found as the difference between the observed and the

calculated pattern was quite small. The lower symmetric orthorhombic *Pnma* (#62) structure of the PMT was authenticated by the Rietveld refinement, which corresponding to the $a^+b^-b^-$ tilt system. The existence of superlattice reflection peaks (011), (210), (230/212), and (311) indicate the disordered orthorhombic structure. The refined parameters were found to be $R_{exp} = 6.77$, $R_p = 5.39$, $R_{wp} = 7.06$ and $\chi^2 = 1.09$. Also, the lattice parameters, which are refined, are found to be $a = 5.5710 \text{ \AA}$, $b = 7.7893 \text{ \AA}$, and $c = 5.4889 \text{ \AA}$. The inset of Fig. 1 shows the PMT unit cell with the sharing of atoms at the Wyckoff positions $4c (x, 1/4, z)$ for Pr^{3+} atoms, $4b (1/2, 0, 0)$ for Mg^{2+} and Ti^{4+} atoms, $4c (x, 1/4, z)$ and $8d (x, y, z)$ for O^{2-} atoms. Each B-site cation (Mg^{2+} or Ti^{4+}) is bonded with six O^{2-} atoms to constitute MgO_6 and TiO_6 octahedra, respectively. The crystallographic refined parameters are tabulated in Table 1. Fig. 1 (b) displays the SEM image of the PMT pellet. The SEM image of PMT discloses the bulks of various sizes and shapes. The domain structure of the PMT with the “lamellae” character is observed. The size of the bulk particles (i.e., grains) varies from $1.25 \mu\text{m}$ to $4.7 \mu\text{m}$.

3.2. LUMINESCENCE STUDIES:

Fig. 2(a) and 2(b) show the photoluminescence excitation (PLE) and emission (PL) spectra of PMT at 300 K (RT), respectively. The PLE spectra are monitored at 200 nm and 613 nm. From Fig. 2(a), it is seen that the PLE spectra consist of two broad bands are located around 277 nm (A band) and 367 nm (B band), are assigned to host absorption of the PMT lattice [26–28] and Pr^{3+} – Ti^{4+} IVCT absorption [29–31], respectively. The PL spectra of PMT show a series of emission peaks in the 400–575 nm range when it is excited with 200 nm, 277 nm (A band), and 367 nm (B band). From the PL spectrum, near Band Edge emission (NBE) was calculated and the band gap energy is found to be 4.48 eV from Tauc plot [Inset of Fig. 2(a)]. From Fig. 2(b), the series of emission peaks consists of a strong band in the range 400–

450 nm, a peak at 470 nm, and a weak band in the range 485–550 nm, which corresponding to ${}^3\text{H}_4 \rightarrow {}^3\text{P}_J$ ($J = 2, 1, 0$), ${}^1\text{I}_6$ ($\sim 400, 415, 422, 438$ nm), ${}^3\text{P}_0 \rightarrow {}^3\text{H}_4$ and ${}^3\text{P}_1, {}^3\text{P}_0 \rightarrow {}^3\text{H}_5$ ($\sim 485, 515$ nm) transitions of Pr^{3+} atoms [32, 33], respectively.

Fig. 2(c) shows the schematic energy level diagram of the PMT. This diagram helps to clearly understand the excitation and recombination processes in PMT. The electrons go to the ${}^3\text{P}_2$ state of Pr^{3+} from its ground state ${}^3\text{H}_4$ upon 400 nm excitation. Then the electrons relax rapidly to ${}^3\text{P}_0$ and ${}^1\text{D}_2$ lower states via IVCT, i.e., the electrons are trapped by Ti^{4+} orbital before they recombine with the holes (h^+) on Pr^{3+} ground state. During the IVCT process, the electrons are excited to Ti^{4+} orbital from the ground state (${}^3\text{H}_4$) of Pr^{3+} and created $[\text{Ti}^{4+}+e^-]$ state [34]. The excited electrons are relaxing to the lowest potential energy of $[\text{Ti}^{4+}+e^-]$ state through a fast non-radiative process. Lastly, the electrons are back to the Pr^{3+} ground state via the excited (${}^3\text{P}_0, {}^1\text{D}_2$) states of Pr^{3+} . In summary, the electron trapping and it recombines with the holes can be written as follows:



where $(\text{Pr}^{3+})^*$ represents excited states of Pr^{3+} atom, (Eq. 1) the light falls on the PMT creates free electron (e^-) and holes (h^+) in the conduction band (cb) and valence band (vb), respectively. (Eq. 2, 3) The electrons are trapped by the Ti^{4+} and creates $[\text{Ti}^{4+} + e^-]$ of Ti^{3+} state, on the other side holes (h^+) are trapped in Pr^{3+} and creates Pr^{4+} state. (Eq. 3, 4) The Ti^{3+} or $[\text{Ti}^{4+} + e^-]$ state releases the cb electron, later which are recombines with the Pr^{4+} and creates the excited $(\text{Pr}^{3+})^*$ state [${}^3\text{P}_J, {}^1\text{D}_2$]. (Eq. 5) Finally, the excited $(\text{Pr}^{3+})^*$ state relaxes to

the ground state [3H_4] of Pr^{3+} , which results in the weak and strong bands in the emission spectra.

The absorption energy of IVCT can be estimated by the following equation [35]:

$$IVCT (cm^{-1}) = 58800 - 49800[\chi(Ti^{4+})/d(Pr^{3+}-Ti^{4+})]$$

where $\chi(Ti^{4+})$ is the optical electro-negativity (2.05) of Ti^{4+} atom; $d(Pr^{3+}-Ti^{4+})$ is the smallest bond length (3.21646 Å) of $Pr^{3+}-Ti^{4+}$ in the PMT lattice, which obtained from Rietveld refinement data. Thus, the absorption energy of IVCT is calculated to be $27060 cm^{-1}$ ($\sim 3.3550 eV \approx 369 nm$), which is approximately similar to the observed data $27248 cm^{-1}$ ($\sim 3.3783 eV \approx 367 nm$) obtained from the PLE spectra. Also, we have calculated the band-gap (E_g) of the PMT using the Tauc plot (direct allowed transition) (Inset of Fig. 2(d)) of UV-vis spectrum (Fig. 2(d)) and the value of E_g is found to be $4.49 eV$ ($\sim 277 nm$), which coincides with the host absorption value (A band) in the PLE spectra.

3.3. FOURIER TRANSFORM INFRARED (FTIR) ANALYSIS:

Fig. 3 shows the FTIR spectrum of PMT. All the peaks and bands are the characteristic of the material except the hump at $1600-2000 cm^{-1}$, which is due to the presence of absorbed moisture in KBr [$KBr.(H_2O)_m$]. The first two peaks at $397 cm^{-1}$ and $419 cm^{-1}$ may be attributed to the asymmetric bending modes of MgO_6 and TiO_6 octahedra respectively. Whereas the peaks at $431 cm^{-1}$ and $457 cm^{-1}$ corresponds to symmetric bending modes of MgO_6 and TiO_6 octahedra respectively. In Fig.3, the inset displays peaks at $570 cm^{-1}$ and $605 cm^{-1}$, which correspond to asymmetric stretching of MgO_6 and TiO_6 octahedra respectively, whereas the two peaks at $930 cm^{-1}$ and $975 cm^{-1}$ may be attributed to the symmetric stretching modes of MgO_6 and TiO_6 octahedra respectively. The small intensity peaks found in the range $1020-1520 cm^{-1}$, likely correspond to the overtones of the

fundamental vibrations in PMT. In FTIR spectra, we generally get two peaks for the two types of octahedra in PMT, which can be explained by the following equation, where the wavenumber of transmittance ($1/\lambda$) can be expressed as

$$\frac{1}{\lambda} = \frac{\nu}{c} = \frac{1}{2\pi c} \sqrt{\frac{k}{\mu}}$$

where k is the molecular force constant, c is the speed of light in the vacuum (i.e., 299792458 m/s) and μ is the reduced mass of the Ti/Mg–O system. The reduced masses for Ti–O and Mg–O bonds which come out to be 11.9911u and 9.648u respectively, where 1u = $1.660539040(20) \times 10^{-27}$ kg. As the reduced mass of Ti–O bonds are larger than Mg–O bonds, therefore the transmittance peaks appear in the lower wavenumber side for Ti–O bonds.

3.4. CONDUCTIVITY ANALYSIS:

The ac conductivity data was measured over the temperature range 300 (RT) – 700 K. The variations of ac conductivity with the frequency (ν) at various temperatures are shown in Fig. 4(a). In the measured frequency range, the ac conductivity spectra show two different regions, which are due to the effects of grain-boundaries (Gb) at low frequency (Region I) and that of bulks at high frequency (Region II) [36]. The dc conductivity value (σ_{dc}) can be estimated by extrapolating conductivity spectra at $\nu = 0$. The whole ac conductivity shows a movement towards the high-frequency side with the increasing temperature. We have adopted the double power law to fit the conductivity spectra and highlight the contributions of Gbs and bulks [36]

$$\sigma_{ac} = \sigma_{dc} + A\omega^{k_1} + B\omega^{k_2} \quad (6)$$

where A , B are the temperature-dependent constant, whereas k_1 , k_2 are the material-dependent parameters. The fitted ac conductivity spectra for 700 K are shown in Fig. 4(a). The fitted parameter values are tabulated in Table 2.

Fig. 4(b) shows the temperature-dependent σ_{dc} for PMT, which shows a decrease in σ_{dc} with increasing temperature suggesting the semiconducting nature of PMT. The values of σ_{dc} are collected from the previous fitted values of σ_{ac} and found approximately the same when matched with the observed data of σ_{dc} . In Fig. 4(c), the values of σ_{dc} are fitted using the nearest-neighbor hopping (NNH) model, defined as,

$$\sigma_{dc} = \sigma_{\alpha} \exp\left(-\frac{E_a}{k_B T}\right) \quad (7)$$

where σ_{α} is the pre-exponential constant, Boltzmann constant (k_B), the activation energy (E_a), and the temperature (T). It is seen that the observed data of σ_{dc} at the high-temperature region is well fitted by Eq. 7, whereas at 400 K, a change in its linear behavior is found, which suggests another dissimilar hopping mechanism in this low-temperature region (below 400 K). From the linear behavior in Fig. 4(c), the value of E_a is obtained and found to be 0.33 eV, which suggesting polaronic conduction between the nearest neighboring atoms [37]. To investigate the type of hopping mechanism below 400 K, the value of E_a at each temperature is calculated with the equation $E_a = -d(\ln\sigma)/d(1/k_B T)$ [38] and the inset of Fig. 4(c) shows the temperature variation of E_a . It is found that the value of E_a decreases to 0.275 eV from its initial value of 0.33 eV with the decrease in the temperature below 400 K, which suggests the range of hopping distance is large than the nearest-neighbor distance due to decreasing activation energy. This decreasing trend of activation energy suggests the disordered states of PMT due to charge imbalance or IVCT between Pr^{3+} and Ti^{4+} in sample.

In this point of view, Mott's variable-range hopping (MVRH) is adopted to fit the values of σ_{dc} in the lower temperature region due to disordered states of PMT are shown in Fig. 4(d). [39, 40]

$$\sigma_{dc} = \sigma_{\beta} \exp \left[- \left(\frac{T_0}{T} \right)^{\frac{1}{4}} \right] \quad (8)$$

where σ_{β} is the pre-exponential constant and the characteristic temperature (T_0). The value of T_0 can also be defined as follows:

$$T_0 = \frac{18}{k_B N(E_F) \xi^3} \quad (9)$$

where the $N(E_F)$ is the density of states at the Fermi energy and ξ be the localization length. The fitted parameter T_0 is found to be 669348164 K. The hopping energy E_h is given by $\frac{1}{4} k_B T^{\frac{3}{4}} T_0^{\frac{1}{4}}$ [41]. It is found that the E_h increases to 0.31 eV from 0.25 eV [inset of Fig. 4(d)]. By adopting a projected value (2.2 Å) of ξ [41], the $N(E_F)$ value is measured to be $2.93 \times 10^{25} \text{ eV}^{-1} \text{ m}^{-3}$, suggesting a higher concentration of charge carriers as reported in a similar type of materials [41]. The hopping distance R_h is also calculated by $\frac{3}{8} \xi \left(\frac{T_0}{T} \right)^{\frac{1}{4}}$ [42] and it is decreasing to 2.967 nm from 3.188 nm with the increasing temperature. From these results, we can conclude that the σ_{dc} points towards a transition from NNH to MVRH around 400 K with the decrease in E_a .

3.5. DIELECTRIC CONSTANT:

Fig. 5(a) and 5(b) shows the frequency variation of dielectric constant (ϵ') and dielectric tangent loss ($\tan\delta$) in the temperature range of 300–700 K. One dispersion region is observed in Fig. 5(a) and also one prominent relaxation peak in $\tan\delta$ is present in the measured frequency range, which indicates the contribution of bulks in the material. On the low-frequency side, the tail of another relaxation process is observed due to Gbs contribution, which is not observed at RT data (300 K). This suggests only bulks contribution dominates the dielectric data at 300 K in the measured frequency range, whereas above RT, the Gbs

contribution is also present along with the bulk contribution. This ϵ' dispersion region and the corresponding $\tan\delta$ peak move towards the high-frequency side with the increase in temperature, which suggests a thermally activated process. The charge carriers' mobility and the temperature strongly dominate the $\tan\delta$ peaks. So, the mobility is increased with the increase in temperature, which results in the movement of $\tan\delta$ peak towards the high-frequency side. The values of $\tan\delta$ peaks for bulks is around 0.25 - 0.5, which is observed above 10^3 Hz and that for *Gbs* is greater than 0.5 at the low-frequency side. A similar value of $\tan\delta$ peak for bulks is reported in various literatures [43, 44].

Fig. 5(c) shows the variation of dielectric constant (ϵ') with the temperature of PMT at various frequencies. It is observed that the values of ϵ' increases with the temperature. As the number of charge carriers increases with the increasing temperature, which helps increase in polarization, results increase in ϵ' value also. The ϵ' values increases stair-like with the temperature (Inset of Fig. 5(c)), which is due to the presence of two microstructural effects (i.e., bulks and *Gbs*) in the material, it is quite similar in the materials with a high dielectric constant [45-50]. Here, *Gbs* have higher capacitance than that of bulks. This *Gbs* creates a highly capacitive layer to traps more charge carriers, which results in a high ϵ' above RT at the low-frequency side [51, 52].

The variation of relaxation times (τ) with temperature are plotted in Fig. 5(d) by utilizing the NNH model.

$$\tau = \tau_0 \exp\left(\frac{E_a}{k_B T}\right) \quad (10)$$

where τ_0 is the pre-exponential factor. The values of τ are collected from the $\tan\delta$ peak positions in Fig. 5(b). These peak positions are collected only for bulks' contribution as the $\tan\delta$ peaks for *Gbs* are not observed in the measured frequency range. From Fig. 5(d), it is observed that the points (τ values) fit well with the straight line, and the value of E_a is found

to be 0.25 eV for this region. On the low-temperature side, the τ values deviate the straight-line fit suggesting the presence of another mechanism below 400 K. In this low-temperature region, we have employed the MVRH model (Inset of [Fig. 5\(d\)](#)) using the equation as given below:

$$\tau = \tau_{\alpha} \exp(T/T_0)^{1/4} \quad (11)$$

where τ_{α} is also a pre-exponential constant. We have seen that a good agreement between the τ values and MVRH is obtained. This result supports the outcomes from dc conductivity data as discussed in [Sec.3.4](#).

3.6. IMPEDANCE ANALYSIS:

The complex impedance plane plots (i.e., Z-plot) for PMT at various temperatures are shown in [Fig. 6\(a\)](#) & [6\(b\)](#). The Z-plot shows one depressing semicircular arc with the tails of another semicircular arc suggesting the presence of two different microstructural effects in PMT. From [Fig. 6\(a\)](#) & [6\(b\)](#), it is seen that the diameter of semicircular arcs are decreasing with the temperature, which throws light on the semiconducting behaviour of sample. As discussed in [Sec. 3.5](#), the *Gbs* is less conducting than bulks, so that the contribution of bulks always lies at relatively high frequencies in the material. The decrease in diameter of these semicircular arcs with the increase in temperature also suggests the thermally activated process [\[52\]](#). The depressed semicircular arcs with the center below X-axis suggest the non-ideal capacitance in PMT. So, we have employed the constant phase element (CPE) model to fit these Z-plots. The non-ideal capacitance of the CPE model can be assumed as $C_{CPE} = Q^{1/n} R^{(1-n)/n}$, where n ($0 \leq n \leq 1$) is a constant that depends on the non-ideal behavior of the capacitance. Here Q and R are the constant phase element and resistance. In [Fig. 6\(a\)](#) and [6\(b\)](#), the observed data (color points) are fitted with the electrical circuit as shown in the inset

of Fig. 6(a). The temperature variation of fitted parameter n is shown in the inset of Fig. 6(b) and the n values increase to 0.995 at 700 K from 0.96 at 300 K (RT). This suggests the bulk capacitance approaches to ideal behavior with an increase in temperature, which may be due to the removal of defects in the bulk interior. The fitted resistance R decreases with an increase in temperature suggesting the semiconducting behavior of PMT.

To study the hopping mechanism from impedance data, we have also plotted the fitted parameter R using the NNH model (Eq. 12) as shown in Fig.6(c).

$$R = R_{\alpha} e^{\left(\frac{E_{\alpha}}{k_B T}\right)} \quad (12)$$

where R_{α} is a pre-exponential constant. The observed (R) points also fit well with the straight line above 400 K with a corresponding E_{α} value is 0.235 eV for the bulks. We have found small differences in the activation energies from dc conductivity, relaxation time, and impedance data. As the hopping energy of the charge carriers are responsible for relaxation and impedance, whereas the disorder and binding energy of polarons along with the hopping energy are involved in the hopping mechanism [53-55]. From these results, we can summarize that similar charge carriers are responsible for the conduction, relaxation, and impedance process. The deviation of points (R -values) from the straight line suggests the presence of another hopping mechanism below 400 K in PMT. In this region, we have also employed the MVRH model (Fig. 6(d)) using the equation given below:

$$\ln(R/R_0) = (T/T_0)^{1/4} \quad (13)$$

where R_0 is a constant value of R . The MVRH model fits well with the fitted R -values, which also supports the outcomes from dc conductivity and relation time data as discussed Sec. 3.4 & 3.5.

3.6. PHOTOCATALYTIC ACTIVITY:

To study the photocatalytic activity of PMT, the photocatalytic degradation of the organic dye rhodamine B (Rh-B) was performed as per literature [56]. Fig. 7(a) shows the changes in absorbance peak around 550 nm with time in presence of UV-light for a maximum of 75 min. The color of the Rh-B solution changes with time and it became colorless after 75 min in presence of both UV-light irradiation and the PMT. Similar experiments were carried out in absence of UV-irradiation with the sample and the presence of UV-irradiation without the sample PMT. The percentage (%) of degradation was defined as $((C_0 - C)/C_0) \times 100\%$, where C_0 is the Rh-B solution's initial concentration and C is the Rh-B solution's concentration during the photocatalytic reaction. From Fig. 7(b), it is found that the degradation (%) of the PMT was about 71%, whereas 0.9% and 3.3% degradations were found in absence of UV-light and PMT, respectively after 30 min. The kinetic behavior of Rh-B degradations are analyzed to understand the photocatalytic efficiency of the PMT sample. The reaction kinetics can be described in terms of first-order kinetics as following [57, 58]:

$$\ln \frac{C}{C_0} = -K_a t \quad (14)$$

where the apparent rate constant (K_a) is the fundamental kinetic parameter for various photocatalysts. Fig. 7(c) shows $\ln \frac{C}{C_0}$ against the time graph and the value of K_a is found to be 0.05058 min^{-1} . For the industrial application, it is important to check the photocatalytic efficiency of the recycled and reused PMT by several times. The photocatalytic efficiency (% degradation) of PMT for 5 times reuses were 98, 96.8, 94.6, 93.9, and 91.2% after 75 min of reaction time, respectively (Fig. 7(d)). No leaching for Pr, Mg or Ti into water was found even after 5th cycle of experiment. There is no change in structural and PL behavior of PMT after each experiment.

In summary, the photocatalytic activity in the PMT can be described based on band alignment as follows:



(Eq. 15) The electrons in the vb can be excited to the cb , with the same number of holes in the vb upon UV irradiation. The electrons are trapped by Ti^{4+} and the holes by Pr^{3+} in the PMT. This charge carrier separation results increase in carrier lifetime due to less charge recombination rate. As a result, more hydroxyl OH^* radicals are created by the reaction of trapped holes and electrons (Eq. 16, 17, 18, 19, 20). These strong oxidizing agents OH^* radicals decompose the organic Rh-B dye (Eq. 21) results in colorless solutions. Therefore, $\text{Pr}^{3+} - \text{Ti}^{4+}$ channel in PMT opens a new route to increase charge carriers' lifetime as well as less recombination rate.

3.7.DENSITY OF STATES AND BAND STRUCTURE:

The spin-polarized DoS of PMT unit cell is calculated using the GGA+U approximation is shown in Fig. 8(a). Also, for the knowledge about the individual contribution of Pr 4*f*, Pr 4*d*, Ti 3*d*, and O 2*p* states to the total DoS, the partial DoS of these states are shown in Fig. 8(b) – 8(d). The calculated band-gap (E_g) is found to be 3.58 eV in Fig. 8(a) when the Fermi

energy (E_F) is set at 0 eV. In PMT, the up-spin and down-spin channels are specified by \uparrow and \downarrow , respectively. The spin-polarized band structures along with total DoS of PMT are shown in Fig. 9. The band structure on the right-hand side (red) is for the up-spin channel, whereas the band structure on the left-hand side (blue) is for the down-spin channel. It is found that the PMT shows a direct band-gap between conduction band minimum and valence band maximum at Γ -point for both up-spin and down-spin channels. The up-spin valence band is composed of Pr 4f/4d and O 2p states with a small contribution of Ti 3d state. On the downside, the O 2p state mainly contributes to the down-spin valence band with a smaller contribution of Ti 3d state. It is also observed that the O 2p state mainly contributes at the valence band maximum near 0 eV, whereas the contribution of Pr 4f/4d and Ti 3d states are nearly zero. The up-spin and down-spin conduction bands are consisting of Pr 4f/4d, Ti 3d, and O 2p states, but the Ti 3d (t_{2g} and e_g) states mainly dominate the conduction band minimum with a smaller contribution of O 2p orbital. It is also observed that Ti 3d state splits into t_{2g} and e_g states by the crystal field formed by oxygen octahedra, with t_{2g} state at lower and the e_g at higher energy levels. So, the partial DoS of all states showing light on the bonding structure of PMT. The O 2p orbital mainly contributes at valence band maximum, whereas Ti 3d orbital at conduction band minimum, which suggesting the hybridization of Ti 3d and O 2p orbitals in PMT. The calculated band-gap (3.58 eV) is found to be smaller than the experimental band-gap (4.49 eV) in Sec. 3.2.

4. CONCLUSIONS:

In this work, the Rietveld refinement was performed on the observed X-ray diffraction (XRD) data, which authenticates the lower symmetric orthorhombic $Pnma$ structure of solid-state synthesized PMT. The Pr^{3+} - Ti^{4+} intervalence charge transfer process plays an important role inside PMT. The ac conductivity spectra are analyzed based on

double power law. The dc conductivity shows a change in the hopping mechanism from NNH to MVRH due to the activation energy reduction. This change in the hopping mechanism is well supported by both the relaxation time and fitted R from Z-plots in PMT. The constant phase element (CPE) model is utilized to fit Z-plots. The bulk capacitance approaches ideal behavior with an increase in temperature, which is due to the removal of defects in the bulk interior. The same type of charge carrier is responsible for the conduction, relaxation, and impedance process. The photocatalytic activity of PMT was performed under UV irradiation with the help of degradation kinetics of rhodamine B. Also, the photocatalytic efficiency of recycled and reused PMT is found 91.2% after the 5th cyclic run, which is an important parameter for the industrial application. The calculated band-gap of PMT is found to be 3.58 eV.

5. CONFLICT OF INTEREST

There is no conflict of interest exists.

6. ACKNOWLEDGMENT

MR (NET JRF, ID no. 522407) acknowledges the financial support provided by the University Grants Commission (UGC), India.

7. DATA AVAILABILITY STATEMENT

The data that support the findings of this study are available from the corresponding author upon reasonable request.

REFERENCES

- [1] C. S. Lan, W. N. Kai, and S. Ibrahim, *et al.*, Preparation of Improved p-n Junction NiO/TiO₂ Nanotubes for Solar-Energy-Driven Light Photocatalysis, *Int. J. Photoenergy*, **2013** (2013) 749.
- [2] M. Alhaddab, A. Shawky, La – doped NaTaO₃perovskitenanocrystals supported with α -Fe₂O₃ for sustainable visible-light-driven elimination of ciprofloxacin in water, *Ceramic International*. Doi: 10.1016/j.ceramint.2020.12.183.
- [3] J. Ryu, and W. Choi, Substrate-Specific Photocatalytic Activities of TiO₂ and Multiactivity Test for Water Treatment Application, *J. Environ. Sci. Technol.*, **42** (2008) 294.
- [4] N. Patel, R. Jaiswal, and T. Warang , *et al.*, Efficient photocatalytic degradation of organic water pollutants using V–N-codoped TiO₂ thin films, *Appl. Catal., B*, **150–151**(2014) 74.
- [5] A. Shawky, S. M. El-Sheikh, M. N. Rashed, S. M. Abdo, T. I. El-Dosoqy, Exfoliated kaolinite nanolayers as an alternative photocatalyst with superb activity, *Journal of Environmental Chemical Engineering*, **7** (2019) 103174.
- [6] M. Alhaddab, A. Shawky, Z. I. Zaki, Reduced grapheme oxide-supported PbTiO₃ nanospheres: Improved ceramic photocatalyst toward enriched photooxidation of thiophene by visible light, *Molecular Catalysis*, **499** (2021) 111301.
- [7] A. Shawky, M. Alhaddab, K.S. Al-Namshah, R. M. Mohamed, N. S. Awwad, *Journal of Molecular Liquids*, **304** (2020) 112704.
- [8] P. Péchy, T. Renouard, and S. M. Zakeeruddin, *et al.*, Engineering of Efficient Panchromatic Sensitizers for Nanocrystalline TiO₂-Based Solar Cells, *J. Am. Chem. Soc.*, **123** (2001) 1613.
- [9] H. Klümper-Westkamp, S. Beling, and A. Mehner, *et al.*, Semiconductor TiO₂ Gas Sensor for Controlling Nitrocarburizing Processes, *Met. Sci. Heat Treat.*, **46** (2004) 305.
- [10] J. A. O. Méndez, C. R. López, and E. P. Melián , *et al.*, Production of hydrogen by water photo-splitting over commercial and synthesised Au/TiO₂, catalysts, *Appl. Catal., B*, **147** (2014) 439.

- [11] A. Shawky, R. M. Mohamed, I.A. Mkhaliid, M. A. Youssef, N.S. Awwad, Visible light-responsive Ag/LaTiO₃ nanowire photocatalysts for efficient elimination of atrazine herbicide in water, *Journal of Molecular Liquids*, **299** (2020) 112163.
- [12] A. Shawky, R. M. Mohamed, I. A. Mkhaliid, M. A. Youssef, N. S. Awwad, *J. Mol. Liq.*, **299** (2020) 112163.
- [13] I. A. Mkhaliid, *J. Alloys Compd*, **631** (2015) 298.
- [14] E. García-López, G. Marci, B. Megna, F. Parisi, L. Armelao, A. Trovarelli, M. Boaro, L. Palmisano, *J. Catal*, **321** (2015) 13.
- [15] M.S. Wrighton, A.B. Ellis, P.T. Wolezanski, D.L. Morse, H.B. Abrahamson, D.S. Ginley, *J. Am. Chem. Soc.* **98** (1976) 2774.
- [16] D. A. L. Téllez, D. M. Buitrago, R. Cardona, E. W. Barrera, and J. Roa-Rojas, *J. of Molecular Structure*, **1067**(2014) 205.
- [17] A. M. Srivastava, H. A. Comanzo, M. G. Brik, Luminescence of Bi³⁺ in the double perovskite La₂MgTiO₆, *Optical Materials*, **75** (2018) 809.
- [18] J. Suntivich, K. J. May, H. A. Gasteiger, J. B. Goodenough and Y. Shao-Horn, *Science*, **334** (2011) 1383.
- [19] X. Yin, J. Yao, Y. Wang, C. Zhao, F. Huang, *J. Lumin.*, **132** (2012) 1701
- [20] Y. Li, J. Wang, X. M. Pan, T. Zhou, R. J. Xie, *J. Mater. Chem. C*, **5** (2017) 1022.
- [21] H. Dong, L. D. Sun, C. H. Yan, *Chem. Soc. Rev.*, **44** (2015) 1608.
- [22] A. Abdukayum, J. T. Chen, Q. Zhao, X. P. Yan, *J. Am. Chem. Soc.*, **135** (2013) 14125.
- [23] M. Rudra, S. Halder, S. Saha, A. Dutta, T. P. Sinha, *Mater Chem. Phys.*, **230**(2019)277.
- [24] A. I. Yakimov, T. Wright, C. J. Adkins, and A. V. Dvurechenskii: *Phys. Rev. B*, **51**(1995) 16549.
- [25] AP. Blaha, K. Schwarz, G. K. H. Madsen, D. Kvasnicka, J. Luitz and K. Schwarz, An Augmented Plane Wave plus Local Orbitals Program for Calculating Crystal Properties. Wien2K Users Guide, Wien Techn. Universitat Austria (2008).
- [26] G. Blasse and A. Bril, *J. Chem. Phys.*, **48**(1968) 3652.
- [27] P. Dorenbos, A. H. Krumpel, E. van der Kolk, P. Boutinaud, M. Bettinelli, and E. Cavalli, *Opt. Mater.*, **32**(2010) 1681.

- [28] H. Zhong, X. Li, R. Shen, J. Zhang, J. Sun, H. Zhong, L. Cheng, Y. Tian, and B. Chen, *J. Alloys Compd.*, **517**(2012) 185.
- [29] P. Boutinaud, E. Pinel, M. Oubaha, R. Mahiou, E. Cavalli, and M. Bettinelli, *Opt. Mater.*, **28**(2006) 9.
- [30] P. Boutinaud, R. Mahiou, E. Cavalli, and M. Bettinelli, *Chem. Phys. Lett.*, **418**(2006) 185.
- [31] P. Boutinaud, L. Sarakha, R. Mahiou, P. Dorenbos, and Y. Inaguma, *J. Lumin.*, **130** (2010) 1725.
- [32] S. Zhang, H. Liang, and C. Liu, *J. Phys. Chem. C*, **117**(2013) 2216.
- [33] Y. Wang, V. Tsiumra, Q. Peng, H. Liang, Y. Zhydachevskyy, M. Chaika, P. Dluzewski, H. Przybylinska, and A. Suchocki, *J. Phys. Chem. A*, **123**(2019) 4021.
- [34] S. Mahlik, M. Grinberg, E. Cavalli, M. Bettinelli, and P. Boutinaud, *J. Phys.: Condens. Matter*, **21**(2009) 105401.
- [35] P. Boutinaud, E. Pinel, M. Dubois, A. P. Vink, and R. Mahiou, *J. Lumin.*, **111**(2005) 69.
- [36] K. Funke, *Prog. Solid State Chem.*, **22** (1993)111.
- [37] A. J. Millis, P. B. Littlewood, and B. I. Shraiman, *Phys. Rev. Lett.*, **74**(1995) 5144.
- [38] S. S. N. Bharadwaja, C. Venkatasubramanian, N. Fieldhouse, S. Ashok, M. W. Horn, T. and N. Jackson, *Appl. Phys. Lett.*, **94**(2009) 222110.
- [39] H. Zheng, W. Weng, G. Han, and P. Du, *J. Phys. Chem. C*, **117**(2013)12966.
- [40] N.F. Mott, *Metal-Insulator Transitions*, Taylor and Francis, London, 1990.
- [41] S. Ravi and M. Kar, *Physica B Condens Matter*, **348**(2004) 169.
- [42] R. M. Hill, *Phys. Stat. Solidi A*, **34**(1976) 601.
- [43] J. Liu, C. G. Duan, W. G. Yin, W. N. Mei, R. W. Smith, and J. R. Hardy, *Phys. Rev. B*, **70**(2004) 144106.
- [44] E. Iguchi, N. Kubota, T. Nakamori, N. Yamamoto, and K. J. Lee, *Phys. Rev. B*, **43**(1991) 8646.
- [45] K. S. Cole and R. H. Cole, *J. Chem. Phys.*, **9** (1941) 341.
- [46] K. S. Cole and R. H. Cole, *J. Chem. Phys.*, **10**(1942) 98.
- [47] S. Krohns, P. Lunkenheimer, S. G. Ebbinghaus, and A. Loidl, *J. Appl. Phys.*, **103**(2008) 084107.
- [48] J. Liu, C.-g. Duan, W. N. Mei, R. W. Smith, and J. R. Hardy, *J. Appl. Phys.*, **98** (2005) 093703.
- [49] P. Lunkenheimer, R. Fichtl, S. G. Ebbinghaus, and A. Loidl, *Phys. Rev. B*, **70**(2004) 172102.

- [50] S. F. Shao, J. L. Zhang, P. Zheng, W. L. Zhong, and C. L. Wang, *J. Appl. Phys.*,**99**(2006) 084106.
- [51] A. Karamaker, S. Majumdar, A. K. Sing, and S. Giri, *J. Phys. D: Appl. Phys.*,**42**(2009) 092004.
- [52] N. Biscup, A. de Andres, and J. L. Martinez, *Phys. Rev. B*,**72**(2005) 024115.
- [53] S. Komine, and E. Iguchi, *J. Phys. Chem. Solids*,**68** (2007) 1504.
- [54] E. Iguchi and W. H. Jung, *Phys. Soc. Japan*,**63** (1994) 3078.
- [55] S. Komine and E. Iguchi, *J. Phys.: Condens. Matter*,**16**(2004) 1061.
- [56] H. Yang and J. Yang, *RSC Adv.*,**8** (2018) 11921.
- [57] R. Burch, J. P. Breen, and F. C. Meunier, *Appl. Catal. B*,**39**(2002) 283.
- [58] M. T. Uddin, Y. Nicolas, C. Olivier, T. Toupance, L. Servant, M. M. Muller, H.-J. Kleebe, J. Ziegler, and W. Jaegermann, *Inorg. Chem.*,**51**(2012) 7764.

Manuscript number: **PHYSB-D-20-02735**

Title: **Hopping mechanisms, photoluminescence studies toward highly efficient UV-responsive Pr₂MgTiO₆ photocatalyst.**

Figures:

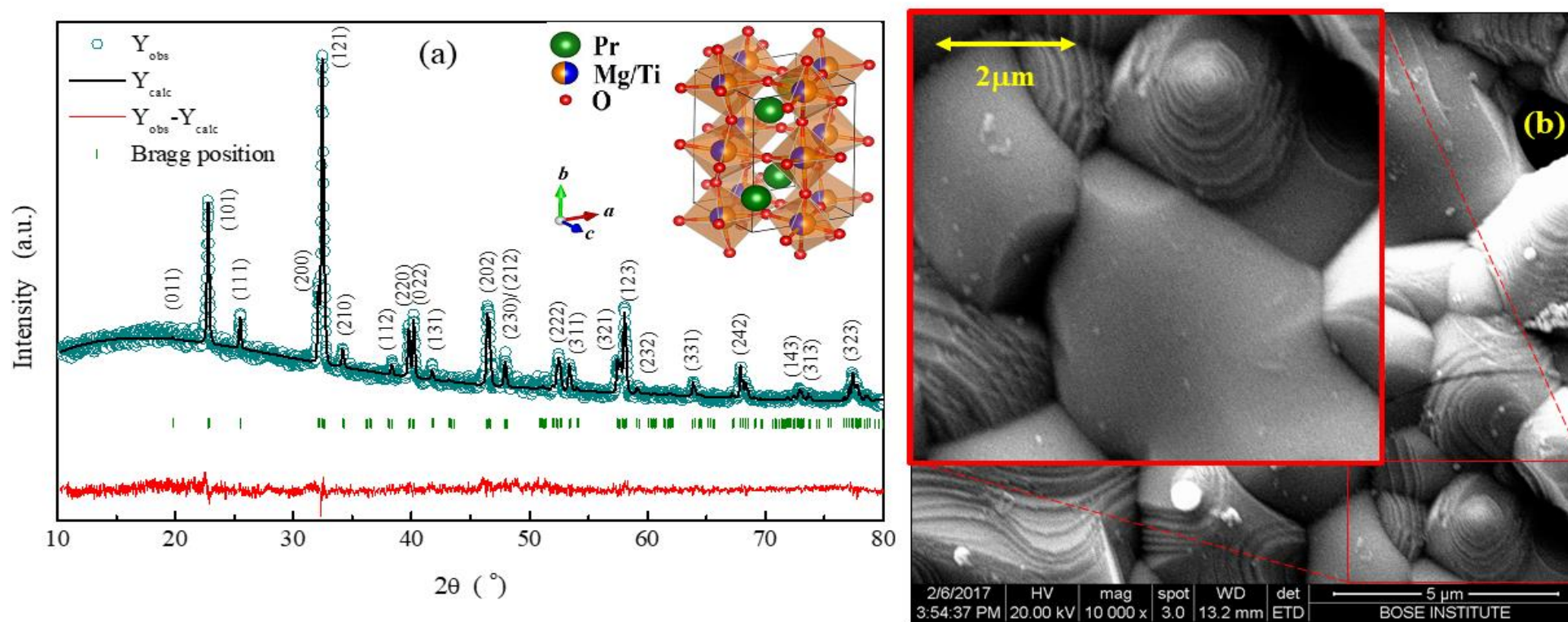


Fig. 1: (a) The X-ray diffraction pattern of PMT at RT, inset shows the unit cell of PMT. (b) The SEM micrograph of PMT.

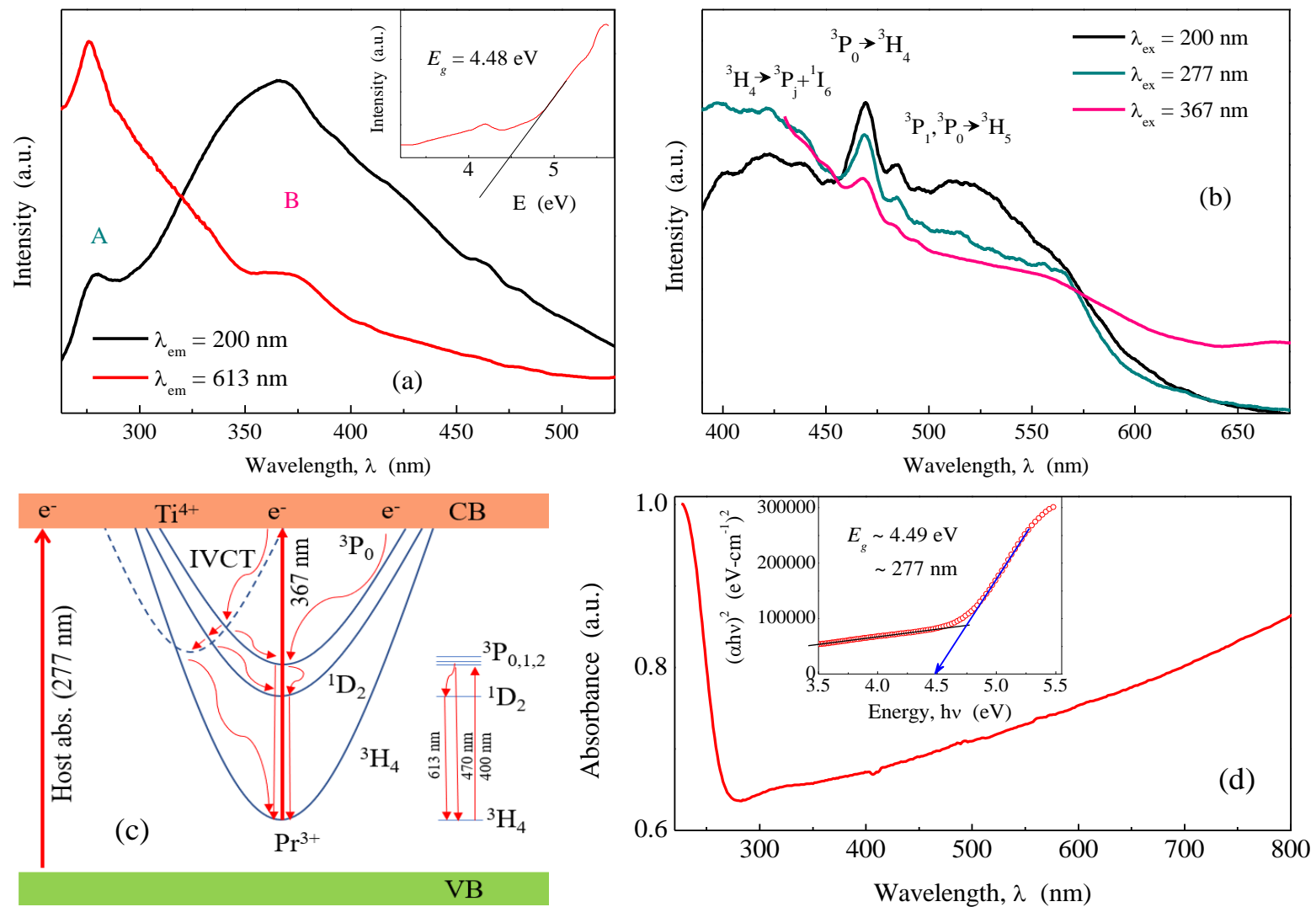


Fig. 2: The photoluminescence excitation (a) and emission (b) spectra of PMT at RT. (c) The schematic energy level diagram of the PMT. (d) The UV-vis absorbance spectrum of PMT and the inset shows the Tauc plot (direct allowed transition) calculated from the UV-vis spectrum.

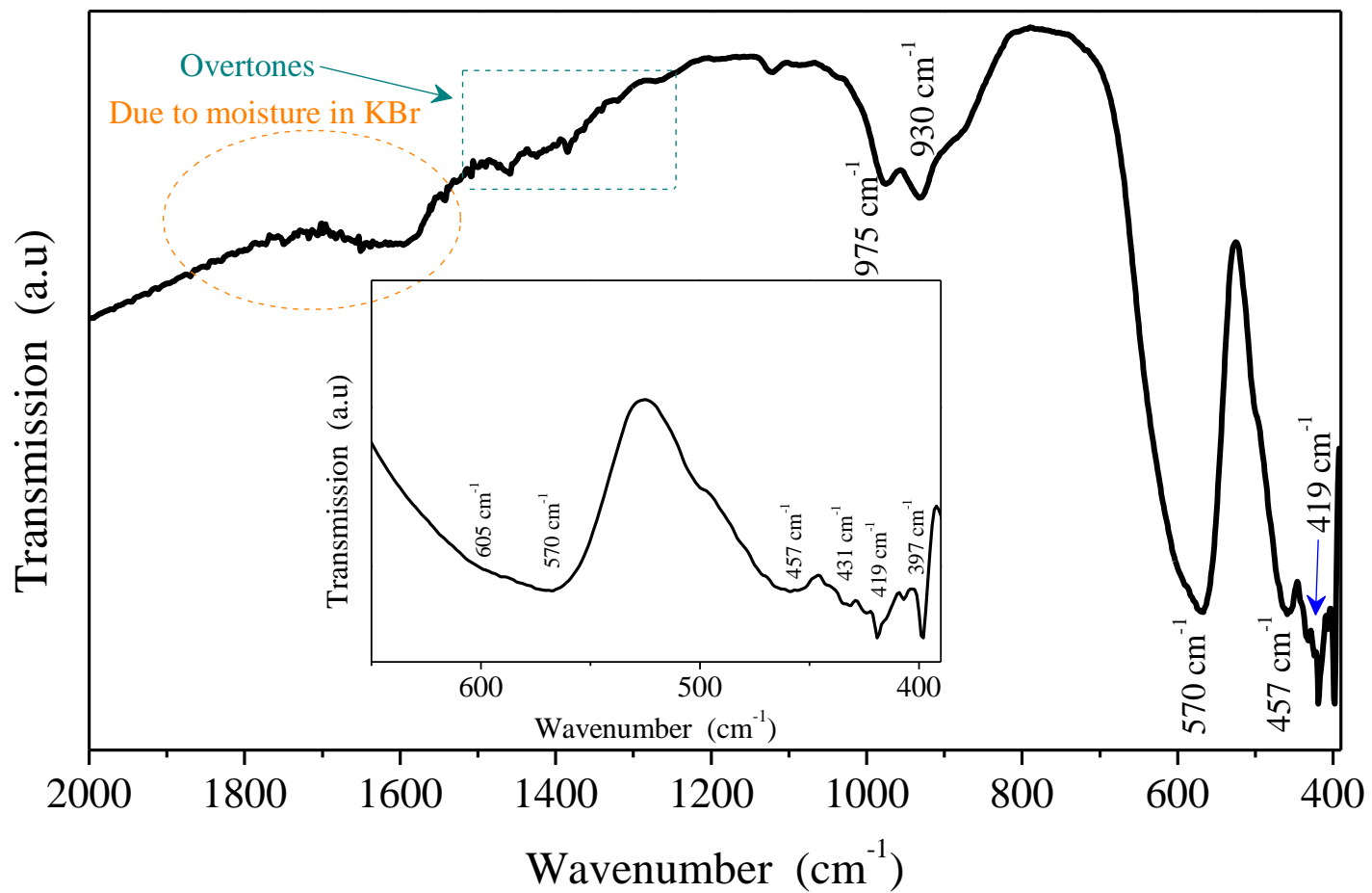


Fig. 3: The FTIR spectrum of PMT.

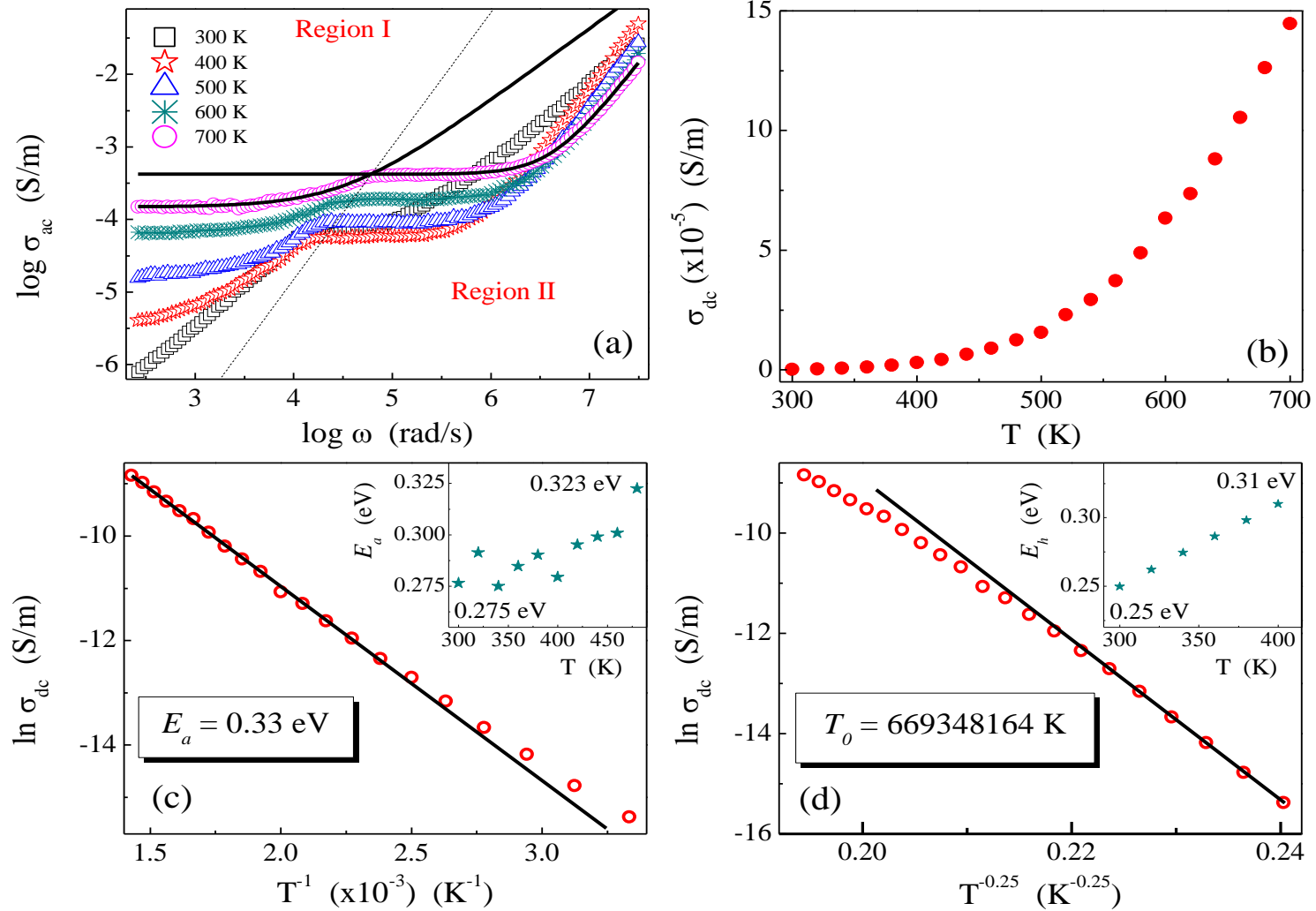


Fig. 4: (a) Frequency dependence of the ac conductivity at various temperatures. (b) The temperature variation of dc conductivity for PMT; The dc conductivity of PMT describes the conduction process using (c) NNH model, (d) MVRH model; The insets show the hopping energy (d) as a function of temperature; (c) Variation of activation energy with the temperature below 400 K.

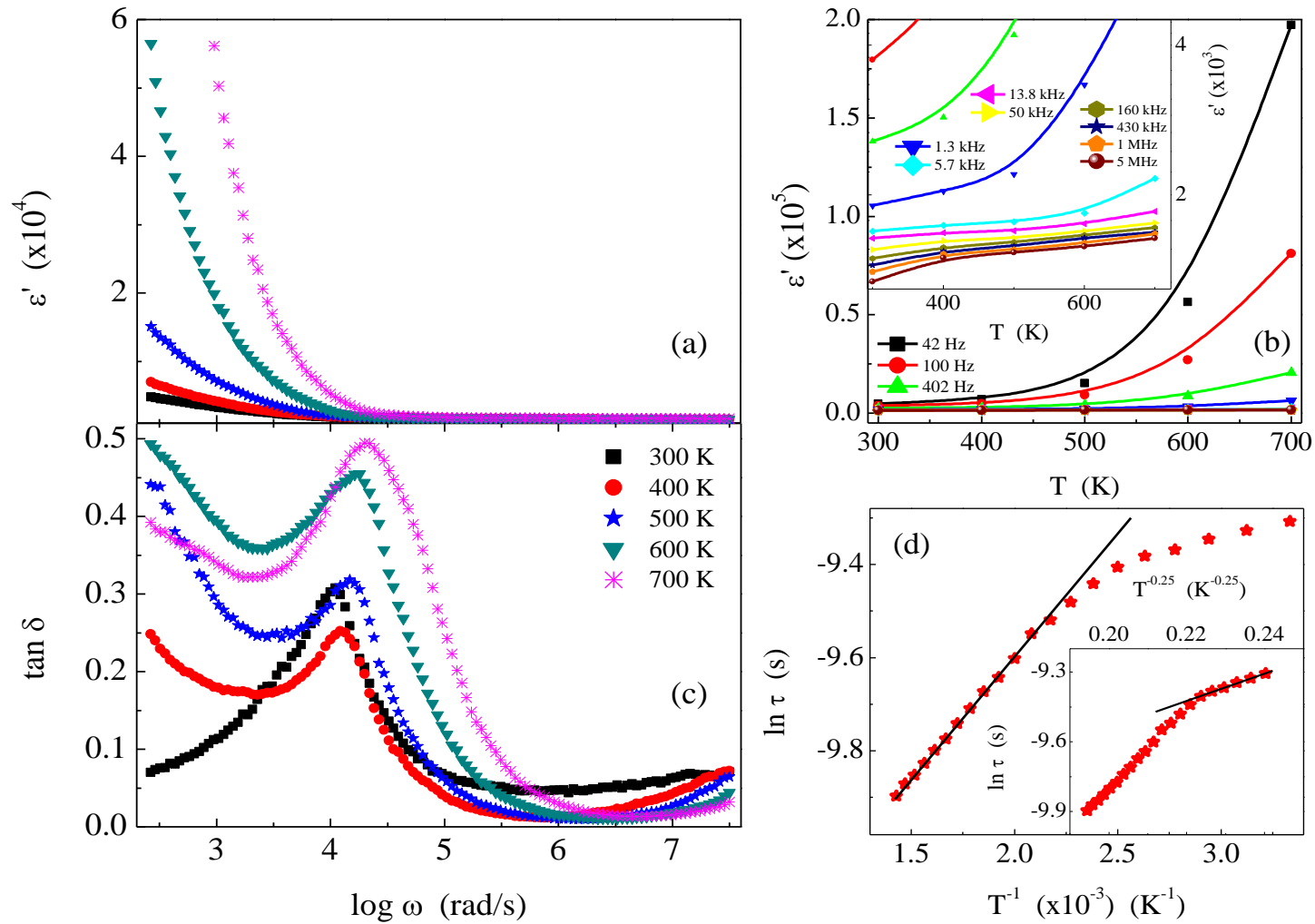


Fig. 5: Frequency dependence of ϵ' (a) and $\tan \delta$ (b) at various temperatures for PMT. Temperature dependence of ϵ' (c) at various frequencies for PMT. Inset (c) shows the closed view of ϵ' with temperature. Relaxation times τ of the charge carriers at bulks are plotted using (d) NNH model and the inset shows τ is plotted using (d) MVRH model.

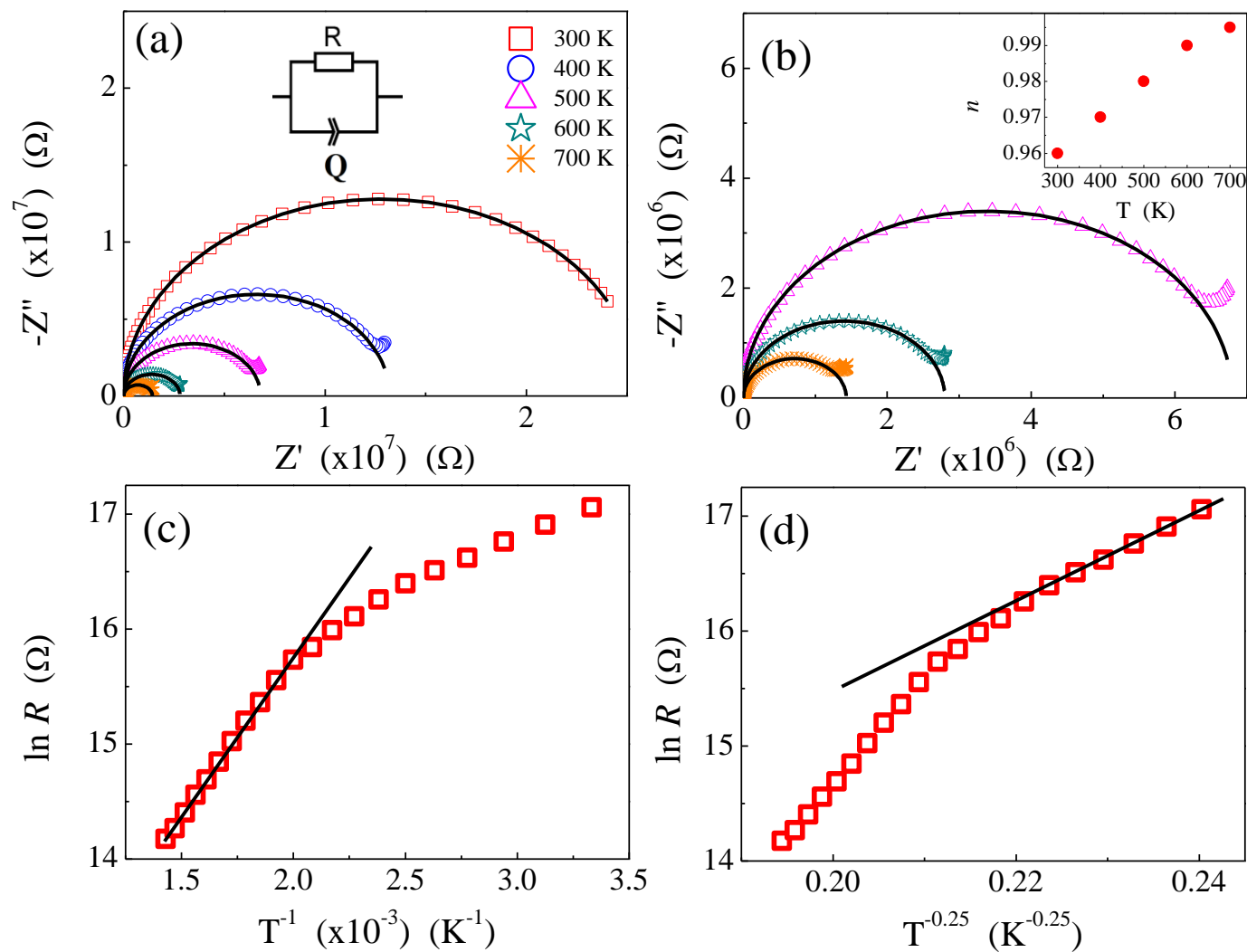


Fig. 6: Z-plots at different temperatures for PMT (a, b). Solid lines are fitted data to the observed data (points). Inset (a) shows the equivalent circuit used to fit the observed data. Inset (b) shows the temperature variation of n . Bulk resistance (R) is plotted using (c) NNH model and (d) MVRH model.

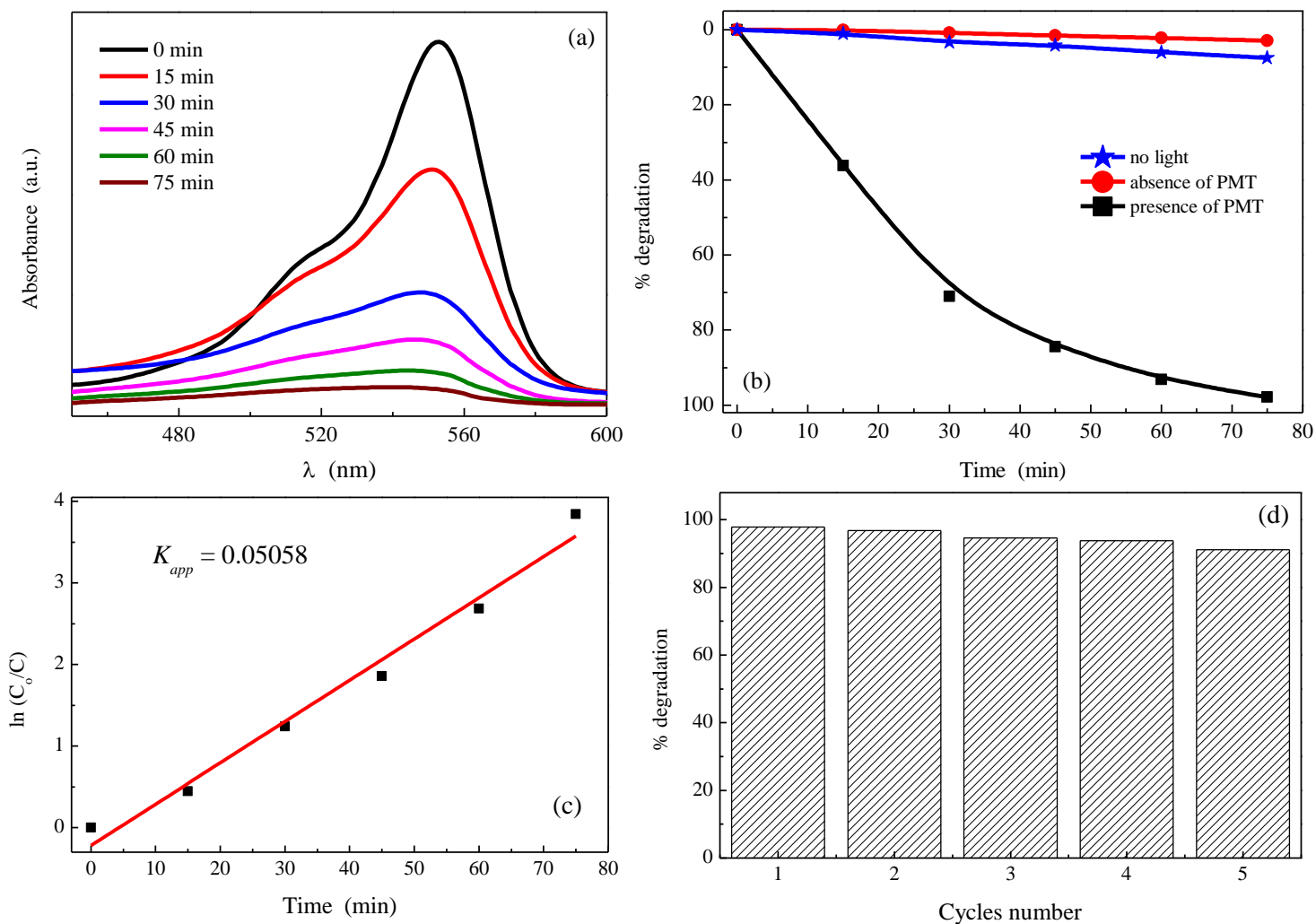


Fig. 7: (a) Change in absorbance of Rh-B solution after different irradiation time in presence of PMT. (b) % degradation of Rh-B in presence of UV only (red circles), PMT in the dark (blue star) and PMT under UV light (black square). (c) $\ln[C_0/C]$ as a function of irradiation time for PMT. (d) Cyclic runs in the %degradation of Rh-B using PMT under UV light.

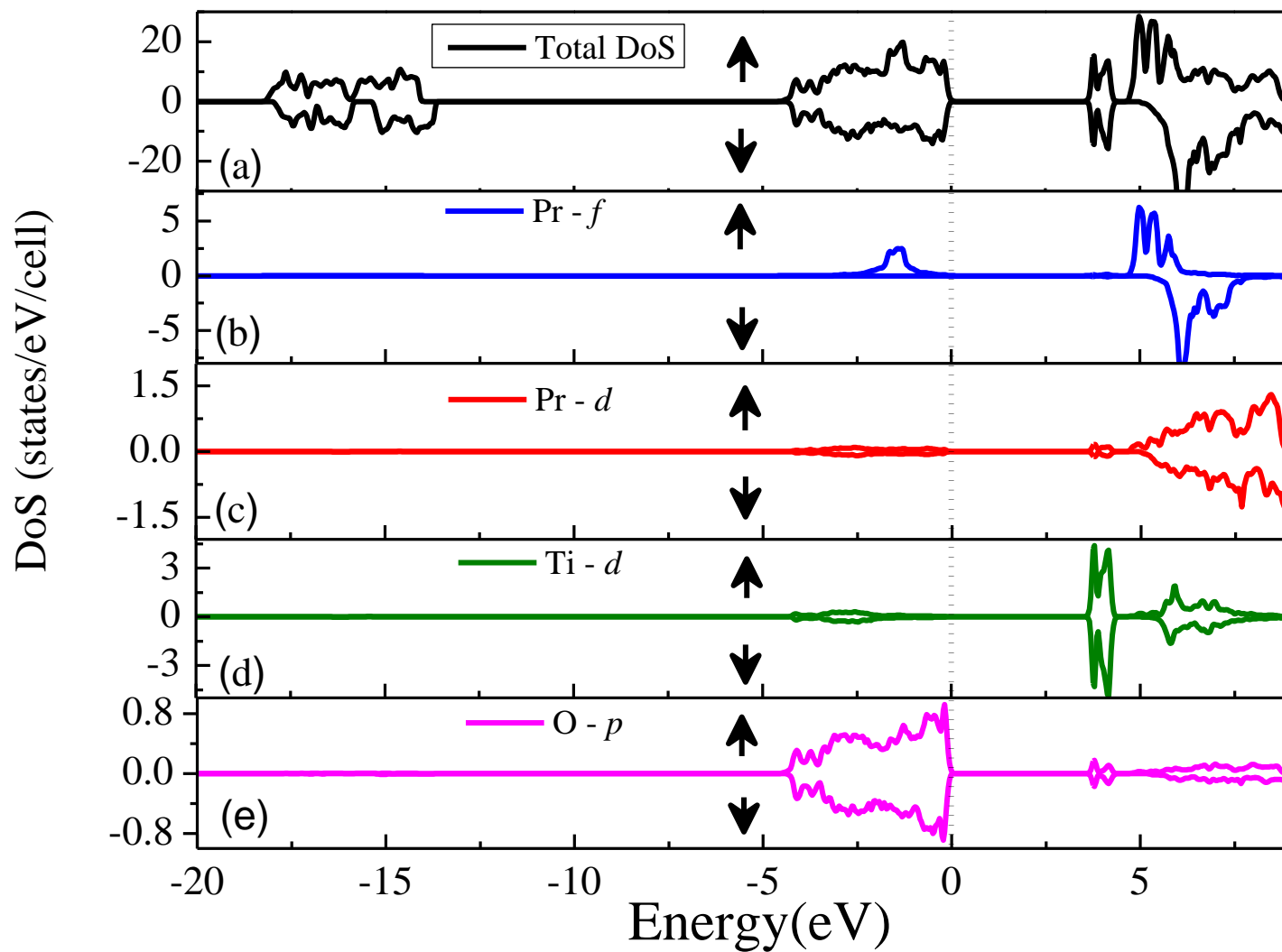


Fig. 8: Calculated total DoS (a) and partial DoS of Pr f (b), Pr d (c), Ti d (d) and O p (e) states of PMT.

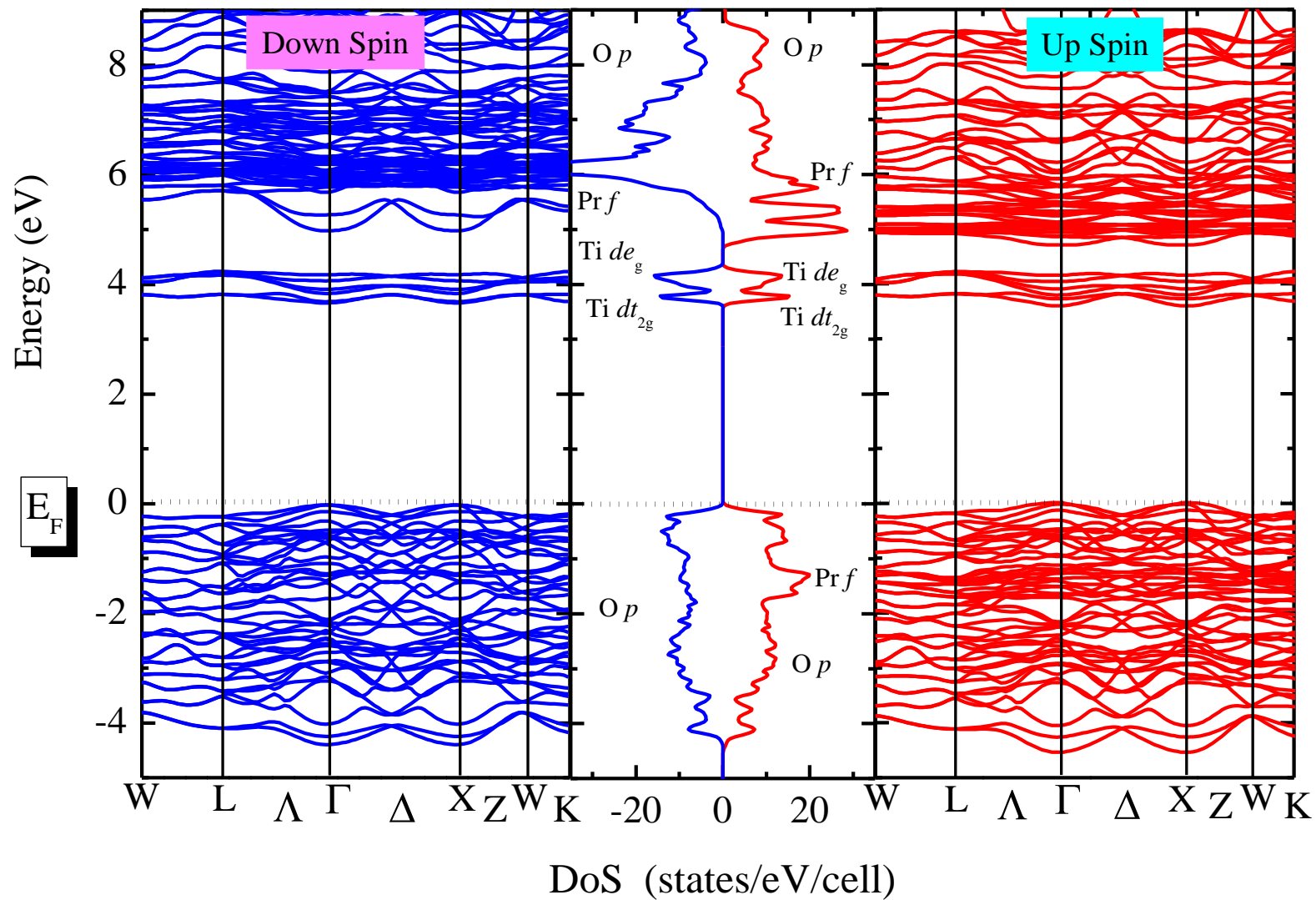


Fig. 9: Band structure for PMT using GGA+U. Bands in red and blue indicate spin up and spin down, respectively.

Figure Captions:

Fig. 1: (a) The X-ray diffraction pattern of PMT at RT, inset shows the unit cell of PMT. (b) The SEM micrograph of PMT.

Fig. 2: The photoluminescence excitation (a) and emission (b) spectra of PMT at RT. (c) The schematic energy level diagram of the PMT. (d) The UV-vis absorbance spectrum of PMT and the inset shows the Tauc plot (direct allowed transition) calculated from the UV-vis spectrum.

Fig. 3: The FTIR spectrum of PMT.

Fig. 4: (a) Frequency dependence of the ac conductivity at various temperatures. (b) The temperature variation of dc conductivity for PMT; The dc conductivity of PMT describes the conduction process using (c) NNH model, (d) MVRH model; The insets show the hopping energy (d) as a function of temperature; (c) Variation of activation energy with the temperature below 400 K.

Fig. 5: Frequency dependence of ϵ' (a) and $\tan\delta$ (b) at various temperatures for PMT. Temperature dependence of ϵ' (c) at various frequencies for PMT. Inset (c) shows the closed view of ϵ' with temperature. Relaxation times τ of the charge carriers at bulks are plotted using (d) NNH model and the inset shows τ is plotted using (d) MVRH model.

Fig. 6: Z-plots at different temperatures for PMT (a, b). Solid lines are fitted data to the observed data (points). Inset (a) shows the equivalent circuit used to fit the observed data. Inset (b) shows the temperature variation of n . Bulk resistance (R) is plotted using (c) NNH model and (d) MVRH model.

Fig. 7: (a) Change in absorbance of Rh-B solution after different irradiation time in presence of PMT. (b) % degradation of Rh-B in presence of UV only (red circles), PMT in the dark (blue star) and PMT under UV light (black square). (c) $\ln[C_0/C]$ as a function of irradiation time for PMT. (d) Cyclic runs in the %degradation of Rh-B using PMT under UV light.

Fig. 8: Calculated total DoS (a) and partial DoS of Pr_f (b), Pr_d (c), Ti_d (d) and O_p (e) states of PMT.

Fig. 9: Band structure for PMT using GGA+U. Bands in red and blue indicate spin up and spin down, respectively.

Manuscript number: **PHYSB-D-20-02735**

Title: **Hopping mechanisms, photoluminescence studies toward highly efficient UV-responsive Pr₂MgTiO₆ photocatalyst.**

Tables:

Table 1: Structural parameters extracted from the Rietveld refinement of the XRD data for PMT.

Space group: <i>Pnma</i> (Orthorhombic)						
Cell parameters: $a = 5.5710 \text{ \AA}$, $b = 7.7893 \text{ \AA}$, and $c = 5.4889 \text{ \AA}$.						
Reliability factors: $R_{exp} = 6.77$, $R_p = 5.39$, $R_{wp} = 7.06$ and $\chi^2 = 1.09$.						
Atoms	Wyckoff site	x	y	z	Bond length (\AA)	Bond angle ($^\circ$)
Pr	4c	0.54063	0.25000	0.51200	Mg–O1 = 2.001(10)	Mg–O1–Ti = 153.3(4)
Mg	4b	0.50000	0.00000	0.00000	Mg–O2 = 1.91(5)	Mg–O2–Ti = 156.2(18)
Ti	4b	0.50000	0.00000	0.00000	Mg–O2 = 2.09(4)	
O1	4c	-0.02601	0.25000	0.41993	Ti–O1 = 2.001(10)	
O2	8d	0.29841	0.03811	0.72531	Ti–O2 = 1.91(5)	
					Ti–O2 = 2.09(4)	

Table 2: Fitted parameters are collected from ac conductivity spectra for PMT.

T(K)	$\sigma_{dc} (\times 10^{-7})$ (S/m)	$A (\times 10^{-9})$	k_1	$B (\times 10^{-14})$	k_2
300	2.09676	0.78	1.2	11000	1.12
400	30.3991	3.9	0.99	0.18	1.79
500	156.261	4.2	0.99	0.13	1.78
600	633.51	5	0.99	0.14	1.75
700	1489.87	5	0.99	0.15	1.73

Table captions:

Table 1: Structural parameters extracted from the Rietveld refinement of the XRD data for PMT.

Table 2: Fitted parameters are collected from ac conductivity spectra for PMT.